Monthly Notices
of the
ROYAL ASTRONOMICAL SOCIETY

MNRAS **484,** 3209–3218 (2019)
Advance Access publication 2019 January 16

doi:10.1093/mnras/stz168

# Low angular momentum relativistic hot accretion flow around Kerr black holes with variable adiabatic index

Indu K. Dihingia,[1] Santabrata Das[1★] and Anuj Nandi[2]

[1] *Indian Institute of Technology Guwahati, Guwahati 781039, India*
[2] *Space Astronomy Group, ISITE Campus, U. R. Rao Satellite Center, Outer Ring Road, Marathahalli, Bangalore 560037, India*

Accepted 2019 January 12. Received 2019 January 12; in original form 2018 September 26

## ABSTRACT

We study the relativistic, time-independent, low angular momentum, inviscid, advective accretion flow around Kerr black hole. Considering the relativistic equation of state (REoS), we examine the transonic properties of the flow and find that there exists an upper bound of the location of the physically accepted critical point ($r_{\rm out}^{\rm max}$). However, no such limit exists when an ideal gas equation of state (IEoS) is assumed to describe the flow. Further, we calculate the global accretion solutions that contain shock waves and separate the domain of parameter space in angular momentum ($\lambda$) and energy ($\mathcal{E}$) plane. We find ample disagreement between the shock parameter spaces obtained for REoS and IEoS, respectively. In general, post-shock flow (equivalently post-shock corona) is characterized by shock location ($r_{\rm s}$) and compression ratio ($R$, measure of density compression across the shock front) which are uniquely determined for flow with given input parameters, namely ($\mathcal{E}$, $\lambda$). Using $r_{\rm s}$ and $R$, we empirically compute the oscillation frequency ($\nu_{\rm QPO}$) of the shock front which is in general quasi-periodic (QP) in nature and retrace the domain of shock parameter space in the $r_{\rm s}$–$R$ plane in terms of $\nu_{\rm QPO}$ for REoS around the weakly as well as rapidly rotating black holes. Finally, we indicate the relevance of this work to explain the plausible origin of high frequency QPO and its connection with the spin ($a_k$) of the Galactic black hole sources.

**Key words:** accretion, accretion discs – black hole physics – hydrodynamics – shock waves.

## 1 INTRODUCTION

Accretion of gas on to a black hole is widely considered to be the underlying source of energy in most energetic astrophysical objects in the universe, namely X-ray binaries (XRBs) and active galactic nuclei (Frank, King & Raine 2002). In general, these objects often exhibit spectral and temporal variabilities in X-rays that eventually carry the imprints of the physical processes active in the accretion flow surrounding the black holes. In particular, the spectral state transitions from low/hard state to high/soft state via intermediate states are observed in black hole XRBs and these sources also display the signature of quasi-periodic oscillations (QPOs) as well (Belloni, Psaltis & van der Klis 2002; Chakrabarti et al. 2002; Homan & Belloni 2005; Remillard & McClintock 2006; Nandi et al. 2012; Iyer, Nandi & Mandal 2015; Nandi et al. 2018).

So far, several efforts were made to understand the origin of the above mentioned X-ray variabilities. Tagger & Pellat (1999) examined the accretion-ejection instability and pointed out that such instability can explain the QPO features. Titarchuk & Osherovich (2000) suggested the global disc oscillation mechanism that possibly causes the persistent QPOs observed in the black hole systems. Ingram & Done (2011) studied the evolution of X-ray timing properties (i.e. QPOs) by means of the fluctuations associated with the hot flows at the inner part of the disc. On the other hand, Svensson & Zdziarski (1994), Esin, McClintock & Narayan (1997), and Done & Kubota (2006) studied the spectral properties of the accretion flow considering Compton corona coupled with the standard Keplerian Disc (Shakura & Sunyaev 1973).

Adopting a self-consistent approach, Chakrabarti and his collaborators (and references therein Chakrabarti & Titarchuk 1995; Mandal & Chakrabarti 2005a,b; Nandi et al. 2012; Debnath, Chakrabarti & Mondal 2014; Iyer et al. 2015; Nandi et al. 2018) have also been investigating both spectral and temporal properties of the Galactic black hole sources since more than two decades where they particularly examine the importance of shock wave in accretion flow. This accretion flow model is developed based on the solution of Two Component Advective Flow (TCAF) paradigm that invokes the role of the post-shock flow (i.e. PSC, equivalent to 'Compton corona'), where due to shock compression, density and temperature become relatively higher compared to the pre-shock flow. In reality, soft photons from the pre-shock flow are intercepted by the hot electrons at PSC and are reprocessed via inverse Comptonization mechanism to produce hard radiations. When PSC modulates, the emergent hard

★ E-mail: sbdas@iitg.ac.in

radiations also oscillate that eventually exhibits QPO features (Das et al. 2014; Suková & Janiuk 2015; Lee et al. 2016). Interestingly, the same PSC region deflects a part of the inflowing matter in the transverse direction of the flow motion to originate bipolar outflows (Chakrabarti 1999; Das et al. 2001a; Das & Chattopadhyay 2008; Aktar, Das & Nandi 2015; Aktar et al. 2017). In the absence of PSC, accretion flow behaves similarly as in the standard thin disc (Shakura & Sunyaev 1973), where outflow generation ceases to exist. Overall, in this model, PSC plays a vital role in determining the emergent flux of the high energy radiations as well as the mass outflow rate from the disc (Chakrabarti & Titarchuk 1995; Nandi et al. 2018).

Meanwhile, the study of the shock waves in the accretion flow around black holes is being carried out by the numerous group of workers both theoretically as well as numerically (Fukue 1987; Chakrabarti 1989; Yang & Kafatos 1995; Molteni, Ryu & Chakrabarti 1996; Ryu, Chakrabarti & Molteni 1997; Lu, Gu & Yuan 1999; Becker & Kazanas 2001; Fukumura & Tsuruta 2004; Das 2007; Kumar et al. 2013; Das et al. 2014; Okuda & Das 2015; Suková & Janiuk 2015; Sarkar & Das 2016; Aktar et al. 2017; Dihingia, Das & Mandal 2018). Very recently, Kim et al. (2017, 2018) showed the formation of shocks in the accretion flow around black holes using general relativistic hydrodynamical numerical simulation. In addition, Nishikawa et al. (2005) and Fukumura et al. (2016) also examined the shock solutions in the GRMHD framework under suitable physical conditions. In general, in an accretion disc, rotating matter experiences centrifugal barrier while falling towards the black hole. Depending on the flow parameters, centrifugal repulsion becomes strong enough to trigger the discontinuous transition of the flow variables in the form of shock waves. Since PSC is formed because of the shock transition, it is generally characterized by the shock variables, namely shock location ($r_s$) and compression ratio ($R$). In a way, both $r_s$ and $R$ are interrelated and also associated with a given accretion solution that harbours shock wave (Das, Chattopadhyay & Chakrabarti 2001b; Das 2007; Chattopadhyay & Kumar 2016; Sarkar & Das 2016; Aktar et al. 2017; Dihingia, Das & Mandal 2018). In addition, in an accretion disc, the flow is expected to be in the thermally relativistic domain (i.e. adiabatic index $\Gamma \rightarrow 4/3$) at the inner part of the disc whereas it remains thermally non-relativistic (i.e. $\Gamma \rightarrow 5/3$) at a distance far away from the black hole horizon (Frank et al. 2002). None the less, for simplicity, $r_s$ and $R$ are generally computed for accretion flows obeying an ideal equation of state (hereafter IEoS), where the value of the adiabatic index ($\Gamma$) remains constant all throughout the flow (and references there in Abramowicz & Chakrabarti 1990; Yang & Kafatos 1995; Chakrabarti 1996; Lu et al. 1999; Das et al. 2001b; Chakrabarti & Das 2004; Fukumura & Tsuruta 2004; Das 2007; Sarkar & Das 2016; Aktar et al. 2017; Dihingia et al. 2018). Recently, Kumar & Chattopadhyay (2017) studied the accretion-ejection solutions using general relativistic prescription; however, no attempts were made to compute the limiting range of $r_s$ and $R$ and their correlation for the relativistic accretion flows around rotating black holes.

Being motivated with these, in this work, we aim to study the structure of the relativistic accretion flows around the Kerr black holes, where inflowing matter is described with a relativistic equation of state (REoS). Here, adiabatic index ($\Gamma$) of the flow no longer remains fixed as it was the case in many earlier works; instead $\Gamma$ is determined here self-consistently based on the thermal properties of the flow (Chattopadhyay & Ryu 2009). To begin with, we consider low angular momentum inviscid transonic accretion flow in the steady state and examine its transonic properties considering both REoS and IEoS. Further, we calculate the shock induced global accretion solutions around rotating black holes and identify the effective region of the parameter space in energy ($\mathcal{E}$) and angular momentum ($\lambda$) plane that permits shock solutions. On comparing the shock parameter spaces obtained for REoS and IEoS, ample disagreement is seen. Further, we empirically compute the frequency of QPO ($\nu_{\rm QPO}$) of the shock front (Chakrabarti & Manickam 2000; Iyer et al. 2015). Since $r_s$ and $R$ are uniquely determined for a shocked accretion flow having fixed ($\lambda$, $\mathcal{E}$), we identify the shock parameter space in $r_s$–$R$ plane in lieu of the canonical $\lambda$–$\mathcal{E}$ plane where we study the two-dimensional projection of three-dimensional plot of $\{r_s, R, \nu_{\rm QPO}\}$. With this, in this work, we study the importance of REoS over IEoS while obtaining the accretion solutions and also investigate the $r_s - R$ correlation for shocked accretion flow around Kerr black holes. Finally, we discuss the implication of the present formalism to study the high frequency QPO (HFQPO) and its possible association with the spin of the Galactic black hole sources.

The paper is organized as follows. In Section 2, we present the governing equations of the relativistic accretion flow. In Section 3, we discuss the critical point analysis. In Section 4, we present the results, where critical point properties, global accretion solutions including shocks, shock properties are discussed. In Section 5, we discuss the astrophysical implication of our formalism. Finally, in Section 6, we present the concluding remarks.

## 2 MODEL EQUATIONS AND ASSUMPTIONS

In this work, the accretion disc around a rotating black hole is considered to be steady, thin, axisymmetric, and non-dissipative in nature. Assumption of inviscid accretion flows around the black hole is supplemented in Appendix A. The black hole is characterized by its mass $M_{\rm BH}$ and spin $a_k = J/M_{\rm BH}$, where $J$ is the angular momentum of the black hole. Throughout the study, we use a unit system as $G = M_{\rm BH} = c = 1$, where $G$ and $c$ are the gravitational constant and speed of light. In this unit system, length, angular momentum, and time are expressed in terms of $GM_{\rm BH}/c^2$, $GM_{\rm BH}/c$, and $GM_{\rm BH}/c^3$, respectively.

### 2.1 Equations of the fluid

The non-dissipative energy momentum tensor for fully ionized fluid is expressed in terms of energy density ($e$), pressure ($p$), and four velocities ($u^\mu$) and is given by

$$T^{\mu\nu} = (e + p)u^\mu u^\nu + pg^{\mu\nu}, \tag{1}$$

where $\mu$ and $\nu$ are indices run from $0 \rightarrow 3$, $g^{\mu\nu}$ are the components of the metric. The conservation of mass flux and the conservation of energy momentum tensor constitute the governing equations of hydrodynamics which are given by

$$T^{\mu\nu}_{;\nu} = 0, \qquad (\rho u^\nu)_{;\nu} = 0, \tag{2}$$

where $\rho$ is the mass density of the flow. Now, we define the projection operator $h^i_\mu = \delta^i_\mu + u^i u_\mu$ that satisfy $h^i_\mu u^\mu = 0$ with '$i$' runs from $1 \rightarrow 3$. This condition helps us to project the Navier–Stokes equation into three vector equations as

$$h^i_\mu T^{\mu\nu}_{0\ ;\nu} = (e + p)u^\nu u^i_{;\nu} + (g^{i\nu} + u^i u^\nu)p_{,\nu} = 0. \tag{3}$$

In addition, the scalar equation which is essentially identified as the first law of thermodynamics is computed as

$$u_\mu T^{\mu\nu}_{;\nu} = u^\mu \left[ \left( \frac{e + p}{\rho} \right) \rho_{,\mu} - e_{,\mu} \right] = 0. \tag{4}$$

In this work, we intend to study the accretion flow around a Kerr black hole and therefore, we chose Kerr metric in Boyer–Lindquist coordinates as

$$\begin{aligned} \mathrm{d}s^2 =& g_{\mu\nu}\mathrm{d}x^\mu \mathrm{d}x^\nu, \\ =& g_{tt}\mathrm{d}t^2 + 2g_{t\phi}\mathrm{d}t\,\mathrm{d}\phi + g_{rr}\mathrm{d}r^2 + g_{\theta\theta}\mathrm{d}\theta^2 + g_{\phi\phi}\mathrm{d}\phi^2, \end{aligned} \tag{5}$$

where $x^\mu (\equiv t, r, \theta, \phi)$ denote coordinates and $g_{tt} = -(1 - 2r/\Sigma)$, $g_{t\phi} = -2a_k r \sin^2\theta/\Sigma$, $g_{rr} = \Sigma/\Delta$, $g_{\theta\theta} = \Sigma$, and $g_{\phi\phi} = A\sin^2\theta/\Sigma$ are the non-zero metric components. Here, $A = (r^2 + a_k^2)^2 - \Delta a_k^2 \sin^2\theta$, $\Sigma = r^2 + a_k^2\cos^2\theta$, and $\Delta = r^2 - 2r + a_k^2$. In this work, we follow a convention where the four velocities satisfy $u_\mu u^\mu = -1$.

To obtain the accretion solutions, one requires to use the equation of state (EoS) describing the relation among the thermodynamical quantities, namely density ($\rho$), pressure ($p$), and internal energy ($e$), respectively. Since the temperature of the accretion flow generally exceeds $\sim 10^{10}$ K at least within few tens of Schwarzschild radius (and references therein Sarkar & Das 2016), in this work, we consider a simplified EoS for REoS consisting of electrons, positrons, and ions (Chattopadhyay & Ryu 2009) and is given by

$$e = n_e m_e f = \frac{\rho}{\tau} f. \tag{6}$$

Here, $\rho = n_e m_e \tau$, $\tau = [2 - \zeta(1 - 1/\chi)]$, $\zeta = n_p/n_e$, and $\chi = m_e/m_p$, respectively, where $n_i$'s and $m_i$'s are the number density and the mass of the species. Throughout this study, we consider the flow to be composed with electrons and ions only and we set $\zeta = 1$, until otherwise stated. Subsequently, the explicit form of $f$ is obtained as

$$f = (2 - \zeta)\left[1 + \Theta\left(\frac{9\Theta + 3}{3\Theta + 2}\right)\right] + \zeta\left[\frac{1}{\chi} + \Theta\left(\frac{9\Theta + 3/\chi}{3\Theta + 2/\chi}\right)\right], \tag{7}$$

where $\Theta (= k_\mathrm{B}T/m_e c^2)$ is the dimensionless temperature. In this context, we define the polytropic index ($N$), adiabatic index ($\Gamma$), and the sound speed ($a_\mathrm{s}$) as

$$N = \frac{1}{2}\frac{\mathrm{d}f}{\mathrm{d}\Theta}; \quad \Gamma = 1 + \frac{1}{N}; \text{and} \quad a_\mathrm{s}^2 = \frac{\Gamma p}{e + p} = \frac{2\Gamma\Theta}{f + 2\Theta}. \tag{8}$$

The essence of REoS is that during accretion, the flow variables determines the $\Gamma$ variation as expected.

It may be noted that because of simplicity, the EoS widely used in the literature is described with a fixed adiabatic index $\Gamma$ (IEoS) and is given by

$$e = \frac{p}{\Gamma - 1} + \rho = \frac{\rho}{\tau} f, \tag{9}$$

where $f = 2N\Theta + \tau$. For the purpose of completeness, it would be worthy to compare results obtained for both REoS and IEoS, respectively.

### 2.2 Governing equations for accretion disc

In this work, since a geometrically thin accretion disc is assumed, it is justified to consider the accreting matter to be confined at the disc equatorial plane. Accordingly, we choose $\theta = \pi/2$ and $u^\theta \sim 0$. Using these conditions, the radial component of the equation (3) takes the form as

$$\begin{aligned} & u^r u^r_{,r} + \frac{1}{2}g^{rr}\frac{g_{tt,r}}{g_{tt}} + \frac{1}{2}u^r u^r\left(\frac{g_{tt,r}}{g_{tt}} + g^{rr}g_{rr,r}\right) \\ & + u^\phi u^t g^{rr}\left(\frac{g_{t\phi}}{g_{tt}}g_{tt,r} - g_{t\phi,r}\right) + \frac{1}{2}u^\phi u^\phi g^{rr} \\ & \times\left(\frac{g_{\phi\phi}g_{tt,r}}{g_{tt}} - g_{\phi\phi,r}\right) + \frac{(g^{rr} + u^r u^r)}{e + p}p_{,r} = 0. \end{aligned} \tag{10}$$

In addition, the continuity equation (second part of equation 2) can be rewritten as the mass accretion rate which is given by

$$\dot{M} = -4\pi r u^r \rho H, \tag{11}$$

where $\dot{M}$ represents the accretion rate that we treat as global constant. Moreover, $H$ refers the local half-thickness of the disc which has the functional form (Riffert & Herold 1995; Peitz & Appl 1997) as

$$H^2 = \frac{pr^3}{\rho\mathcal{F}}, \tag{12}$$

with

$$\mathcal{F} = \gamma_\phi^2\frac{(r^2 + a_k^2)^2 + 2\Delta a_k^2}{(r^2 + a_k^2)^2 - 2\Delta a_k^2},$$

where $\gamma_\phi^2 = 1/(1 - v_\phi^2)$ and $v_\phi^2 = u^\phi u_\phi/(-u^t u_t)$. We define the radial three velocity in the co-rotating frame as $v^2 = \gamma_\phi^2 v_r^2$ and thus we have $\gamma^2 = 1/(1 - v^2)$, where $v_r^2 = u^r u_r/(-u^t u_t)$.

We adopt a stationary metric $g^{\mu\nu}$ which has axial symmetry. This enables us to construct two Killing vector fields $\partial_t$ and $\partial_\phi$ that provide two conserved quantities for the fluid motion in this gravitational field and are given by

$$hu_\phi = \text{constant}; \qquad -hu_t = \text{constant} = \mathcal{E}, \tag{13}$$

where $h\,[= (e + p)/\rho]$ is the specific enthalpy of the fluid, $\mathcal{E}$ is the Bernoulli constant (i.e. the specific energy of the flow) and $u_t = -\gamma\gamma_\phi/\sqrt{g^{t\phi}\lambda - g^{tt}}$, where $\lambda\,(= -u_\phi/u_t)$ denotes the conserved specific angular momentum.

## 3 CRITICAL POINT ANALYSIS

Simplifying equations (4), (6), (10), and (11), we obtain the wind equation in the co-rotating frame as

$$\frac{\mathrm{d}v}{\mathrm{d}r} = \frac{\mathcal{N}}{\mathcal{D}}, \tag{14}$$

where the numerator $\mathcal{N}$ is given by

$$\begin{aligned} \mathcal{N} =& -\frac{1}{(r-2)r} + \gamma_\phi^2\frac{2a_k}{r^2\Delta}\lambda + \gamma_\phi^2\frac{4a_k^2}{(r-2)r^2\Delta} \\ & - \gamma_\phi^2\Omega\lambda\frac{2a_k^2 - (r-3)r^2}{r^2\Delta} + 2a_k\gamma_\phi^2\Omega\frac{(r-3)r^2 - 2a_k^2}{(r-2)r^2\Delta} \\ & + \frac{2a_\mathrm{s}^2}{\Gamma + 1}\left[\frac{(r - a_k^2)}{r\Delta} + \frac{5}{2r} - \frac{1}{2\mathcal{F}}\frac{\mathrm{d}\mathcal{F}}{\mathrm{d}r}\right], \end{aligned} \tag{15}$$

and the denominator $\mathcal{D}$ is given by

$$\mathcal{D} = \gamma^2\left[v - \frac{2a_\mathrm{s}^2}{v(\Gamma + 1)}\right]. \tag{16}$$

Using equation (14) in equation (4), we calculate the derivative of the dimensionless temperature as

$$\frac{\mathrm{d}\Theta}{\mathrm{d}r} = -\frac{2\Theta}{2N + 1}\left[\frac{(r - a_k^2)}{r\Delta} + \frac{\gamma^2}{v}\frac{\mathrm{d}v}{\mathrm{d}r} + \frac{5}{2r} - \frac{1}{2\mathcal{F}}\frac{\mathrm{d}\mathcal{F}}{\mathrm{d}r}\right]. \tag{17}$$

In case of accretion process around the black holes, since the inflowing matter smoothly accretes all throughout starting from the outer edge of the disc (i.e. subsonic) up to the horizon (i.e. suppersonic), the radial velocity gradient (equation 14) must be real and finite always. However, equation (16) indicates that the denominator ($\mathcal{D}$) may vanish at some points and therefore, to keep $dv/dr$ finite, numerator ($\mathcal{N}$) must also tend to zero there. These spatial points where both $\mathcal{N}$ and $\mathcal{D}$ simultaneously tend to zero (i.e. $dv/dr = 0/0$) are called as critical points and the conditions $\mathcal{N} = 0$ and $\mathcal{D} = 0$ are known as critical point conditions. Using condition $\mathcal{D} = 0$, we obtain the expression of Mach number ($M = v/a_s$) at the critical point ($r_c$) as

$$M_c \equiv M(r_c) = \sqrt{\frac{2}{\Gamma_c + 1}}, \tag{18}$$

Setting $\mathcal{N} = 0$, we have

$$v_c^2 = \frac{\mathcal{N}_N}{\mathcal{N}_D}, \tag{19}$$

with

$$\mathcal{N}_N = \left[\frac{1}{(r-2)r} - \frac{2a_k\gamma_\phi^2\lambda}{r^2\Delta} + \frac{\gamma_\phi^2\Omega\lambda\left[2a_k^2 - (r-3)r^2\right]}{r^2\Delta}\right]_c - \left[\frac{4a_k^2\gamma_\phi^2}{(r-2)r^2\Delta} + \frac{2a\gamma_\phi^2\Omega\left[(r-3)r^2 - 2a_k^2\right]}{(r-2)r^2\Delta}\right]_c,$$

and

$$\mathcal{N}_D = \left[\frac{(r-a_k^2)}{r\Delta} + \frac{5}{2r} - \frac{1}{2\mathcal{F}}\frac{d\mathcal{F}}{dr}\right]_c,$$

where subscript 'c' denotes the quantities evaluated at the critical point ($r_c$). By solving equations (18) and (19) with help of equation (8), we calculate $\Theta_c$ and $v_c$ at the critical point. These values serve as the initial conditions to integrate equations (14) and (17). Before integrating these equations, the values of $dv/dr|_c$ need to be determined that eventually provide the essence of the critical point characteristics. It is noteworthy that $dv/dr|_c$ usually assumes two values: when both values of $dv/dr|_c$ are real and of opposite sign, critical points are known as saddle type; if $dv/dr|_c$ takes two value of same sign, critical points are known as nodal type; and the spiral-type critical point is obtained when $dv/dr|_c$ becomes imaginary (Holzer 1977). To calculate $dv/dr|_c$, we employ lH´ospital rule and the explicit expression is obtained as

$$\left.\frac{dv}{dr}\right|_c = \frac{N_1 - D_2 \pm \sqrt{(N_1 - D_2)^2 + 4D_1N_2}}{2D_1}, \tag{20}$$

where $N_1$, $N_2$, $D_1$, and $D_2$ are the functions of the flow variables which are given in Appendix B. It may be noted that saddle type critical points are specially important in accretion disc as they are stable (Kato et al. 1993) and accretion flow smoothly passes through it (Liang & Thompson 1980; Abramowicz & Zurek 1981; Chakrabarti 1989) before entering into the black hole. Thus, in a realistic scenario, accretion flow must contain at least one saddle type critical point. In the subsequent sections, we refer all the saddle type critical points as critical points unless otherwise stated.

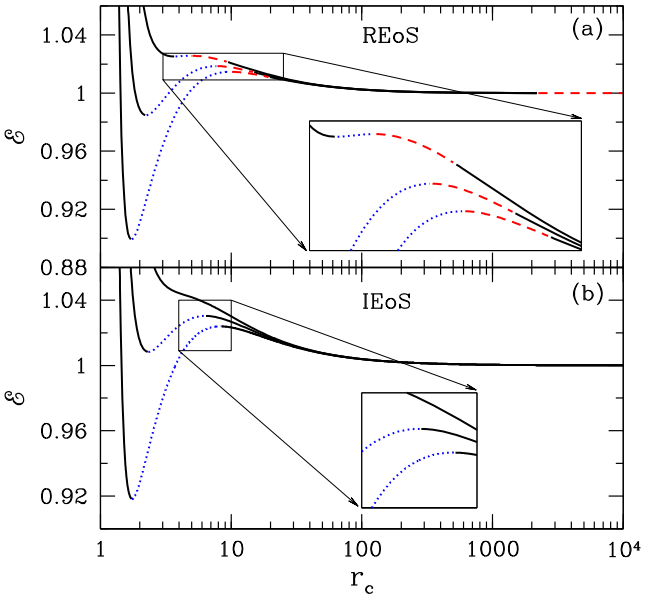


**Figure 1.** Plot of energy at the critical point ($\mathcal{E}$) as a function of critical point location ($r_c$) for three angular momentum $\lambda = 2.00$, 1.90, and 1.80 (bottom to top) in both the panels with $a_k = 0.99$. Here, results presented in the upper and lower panels are for the REoS and IEoS, respectively. For IEoS, we choose $\Gamma = 1.4$. Solid, dash, and dotted curves represent results corresponding to the saddle, nodal, and spiral-type critical points. See text for details.

## 4 RESULTS AND DISCUSSIONS

### 4.1 Nature of critical points

In order to calculate the location of critical points, we solve the second part of equation (13) by supplying the global parameters $\mathcal{E}$, $\lambda$, and $a_k$, respectively. Depending on the choice of the parameters, the flow may contain either single or multiple critical points through which it enters into the black hole (Fukue 1987; Chakrabarti 1989). In this section, we investigate the transonic nature of the accretion flow and in Fig. 1, we present the variation of the flow energy ($\mathcal{E}$) as function of logarithmic critical point locations ($r_c$) for various angular momentum around a black hole having spin $a_k = 0.99$. The obtained results are plotted for REoS and IEoS in the upper panel (Fig. 1a) and lower panel (Fig. 1b), respectively, and in each panel, various curves from top to bottom are for different angular momentums which are given by $\lambda = 1.8$, 1.9, and 2.0, respectively. In case of IEoS, we consider $\Gamma = 1.4$ as a representative value. The solid, dashed, and dotted parts of the curve represent the saddle type, nodal type, and spiral-type critical points. We observe that for REoS, all three types of critical points are present in systematic order: for example, saddle – spiral – nodal – saddle – nodal as the critical point locations are increased. On the contrary, nodal type critical point is absent for IEoS. Moreover, we observe that for a given angular momentum, there exists a range of energy that provides multiple critical points in the flow. Among them, the closest one from the black hole is called as the inner critical point ($r_{in}$), and the furthest one is called as the outer critical point ($r_{out}$). Since only saddle type critical points are physically acceptable, we find an upper limit of outer critical point ($r_{out}^{max}$) for REoS whereas $r_{out}$ remains unbounded for IEoS. Usually, since accretion flow encounters discontinuous shock transition in between $r_{in}$ and $r_{out}$ (Chakrabarti 1989), the maximum possible shock radius ($r_s^{max}$) will have an upper bound for

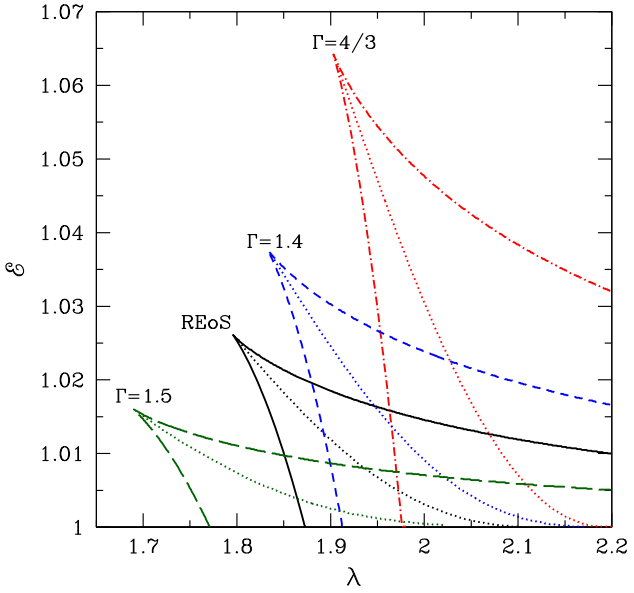


**Figure 2.** Comparison of parameter spaces for multiple critical points in $\lambda$–$\mathcal{E}$ plane. Region bounded by the solid curve is for REoS and the region bounded by dot–dashed, small-dash, and long-dash curves are for IEoS with $\Gamma = 4/3$, 1.4, and 1.5, respectively. The domain of each parameter space is further subdivided using dotted curve that corresponds to accretion solutions having equal entropy at the inner and outer critical points. See text for details.

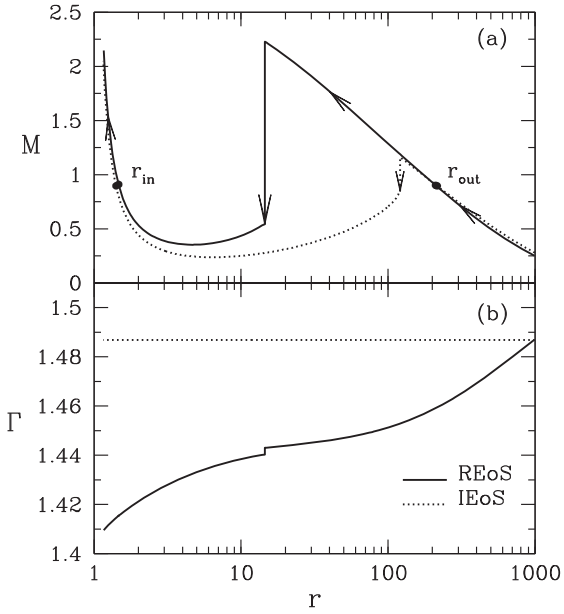


**Figure 3.** Comparison of accretion solutions containing shock waves for REoS and IEoS. In the upper panel (a), variation of Mach number is presented as function of radial coordinate ($r$). Here, input parameters are chosen as $\mathcal{E} = 1.001$, $\lambda = 1.98$, and $a_k = 0.99$, respectively. In both cases, flows are injected at $r = 10^3$ with adiabatic index $\Gamma = 1.4896$. Solid and dashed curves are used to depict the results corresponding to REoS and IEoS. In the lower panel (b), variation of $\Gamma$ is plotted with $r$. See text for details.

REoS. In case of IEoS, since $r_{\rm out}^{\rm max}$ is practically limitless, $r_{\rm s}^{\rm max}$ also becomes unbounded. In reality, the accretion flow remains thermally non-relativistic (i.e. $\Gamma \rightarrow 5/3$) at far away distances from the black hole as the temperature of the accretion flow is small. When the flow proceeds towards the black hole, its temperature increases due to compression and eventually flow becomes thermally relativistic (i.e. $\Gamma \rightarrow 4/3$) at the inner part of the disc. Note that REoS describes the above features of the accretion flow very much satisfactorily and thus we do not find any transonic accretion solution (absence of saddle type critical points) in the non-relativistic regime. These findings are consistent with results reported in Chakrabarti (1990). In case of IEoS, as $\Gamma$ is considered to be constant (and $4/3 \leq \Gamma < 5/3$), $r_{\rm out}$ continues to exist even at the outer edge of the disc. In the inset, we zoom a small part of the curves for clarity purposes only.

### 4.2 Parameter space for multiple critical points

In this section, we study the parameter space in $\lambda$–$\mathcal{E}$ plane for the accretion flow that contains multiple critical points. In Fig. 2, we identify the effective region of the parameter space bounded by the solid curves for REoS whereas the region separated using dot–dashed ($\Gamma = 4/3$), dashed ($\Gamma = 1.4$), and long-dashed ($\Gamma = 1.5$) are obtained for IEoS. Note that all four parameter spaces are further subdivided based on the ratio of entropies ($\eta = \dot{\mathcal{M}}_{\rm in}/\dot{\mathcal{M}}_{\rm out}$) measured at inner and outer critical points. Dotted curve in every parameter space corresponds to $\eta = 1$: above and below the dotted curve we have $\eta < 1$ and $\eta > 1$, respectively. It is also clear that the multiple critical point parameter space for REoS only display a partial overlap with the remaining cases and hence, we point out that any observable computed using IEoS is expected to be erroneous.

### 4.3 Global accretion solution with shock

In the previous section, we have shown that depending on the flow parameters, such as energy ($\mathcal{E}$) and angular momentum ($\lambda$), accretion flow may possess both inner ($r_{\rm in}$) and outer ($r_{\rm out}$) critical points. Interestingly, flow cannot smoothly pass through both critical points simultaneously unless it makes a transition in between them. In actuality, inflowing matter from the outer edge of the disc first crosses $r_{\rm out}$ to change its sonic state from subsonic to supersonic and continues to proceed. Meanwhile, centrifugal repulsion becomes comparable against gravity that causes the accumulation of matter around the black hole. Due to this, a virtual barrier is developed that eventually triggers the discontinuous transition of the flow in the subsonic branch as a shock wave. After the shock, flow velocity gradually increases and again becomes supersonic at $r_{\rm in}$ before falling into the black hole. For shock, the following shock conditions (Taub 1948) are needed to be satisfied which are given by

$$[\rho u^r] = 0, \qquad [(e+p)u^t u^r] = 0,$$
$$\text{and} \quad [(e+p)u^r u^r + p g^{rr}] = 0, \tag{21}$$

where quantities within the square brackets denote their differences across the shock front. In this work, we denote the location of the shock transition as $r_{\rm s}$ which measures the size of the post-shock corona (i.e. PSC). It may be noted that solutions of this kind that passes through $r_{\rm out}$, $r_{\rm s}$, and $r_{\rm in}$ successively are known as global transonic shocked accretion solutions.

In Fig. 3, we compare two typical accretion solutions corresponding to REoS and IEoS where both solutions harbour shock waves. In Fig. 3(a), we depict the variation of Mach number ($M$) with radial distance ($r$) where the input parameters are chosen as $\mathcal{E} = 1.001$, $\lambda = 1.98$, and $a_k = 0.99$, respectively, and subsonic flow is injected

from $r = 10^3$ with $\Gamma = 1.4896$. Results plotted using solid and dotted curves are for REoS and IEoS, respectively. For REoS, the flow becomes supersonic after passing through the outer critical point at $r_{\rm out} = 210.3884$ and continues its journey towards the black hole. Meanwhile, inflowing matter starts experiencing centrifugal repulsion and eventually encounters discontinuous shock transition in the subsonic branch at $r_{\rm s} = 14.5090$ as the shock conditions are satisfied there. This is indicated by the solid vertical arrow. Just after the shock transition, flow momentarily slows down and then gradually picks up its radial velocity due to gravitational attraction. Ultimately, the flow enters into the black hole supersonically after crossing the inner critical point at $r_{\rm in} = 1.4696$. Similar to REoS, we observe the flow to pass through the shock (shown by the dotted arrow) for IEoS also, however, the outer critical point, shock, and inner critical point are obtained at different locations as $r_{\rm out} = 215.5590$, $r_s = 120.5611$, and $r_{\rm in} = 1.4132$, respectively. In Fig. 3(b), we show the profile of adiabatic index ($\Gamma$) as function of $r$. As expected, $\Gamma$ remains constant ($= 1.4869$) all throughout for IEoS whereas it decreases as the flow accretes towards the black hole for REoS. In general, accreting matter is compressed due to shock transition and consequently, density of the flow shoots up across the shock front which is measured by defining the compression ratio as $R = \sigma_+/\sigma_-$, where $\sigma = \rho H$ and '+' and '−' signs denote quantities calculated at immediate post-shock and pre-shock region. In the case of the above two solutions for REoS and IEoS, $R$ is calculated as 2.91 and 1.22, respectively. It may be noted that the location of the shock renders the size of the PSC where the soft photons from the pre-shock flow interact with the hot electrons of PSC via inverse Comptonization process to produce hard radiations (and references therein Nandi et al. 2018). Thus, according to our model, both shock location and compression ratio seem to play a decisive role in determining the spectral features of the accretion disc around the black holes (Chakrabarti & Titarchuk 1995; Mandal & Chakrabarti 2005b). Since the accretion disc structures calculated using REoS and IEoS are not in agreement and REoS is developed based on the physically motivated formalism, we, therefore, point out that it would be appropriate to utilize the accretion solutions yielded from REoS to study the observable properties of the black hole sources.

### 4.4 Parameter space for shock

In this section, we examine the range of the flow parameters, namely energy ($\mathcal{E}$) and angular momentum ($\lambda$) that admits shock induced global accretion solutions around the rotating black holes. In Fig. 4, we identify the effective domain of the parameter space for the shock in the $\lambda$–$\mathcal{E}$ plane where the region bounded by the solid curve is obtained for REoS. In addition, we also separate the shock parameter space for IEoS where dot–dashed, dashed, and long-dashed boundaries denote the results for $\Gamma = 4/3$, 1.4, and 1.5, respectively. In all the cases, we choose $a_k = 0.99$. Clearly, noticeable disagreement is seen among the shock parameter spaces obtained for REoS and IEoSs.

We continue to study the shock parameter space around rotating black hole having different spin values. In Fig. 5, we present the shock parameter space for $a_k = 0.99, 0.9, 0.5, 0.0$, and $-0.99$ (left to right), respectively, where two-dimensional projection of the three-dimensional plot spanned with $\lambda$, $\mathcal{E}$, and $r_{\rm s}$ is shown. In the figure, vertical colour-coded bar in the right side refers the range of $r_{\rm s}$ calculated using REoS where we obtain the minimum value of shock location as $r_{\rm s}^{\rm min} = 3.7314$ and the maximum value of shock location as $r_{\rm s}^{\rm max} = 1071.5519$. We observe that the effective bounded region

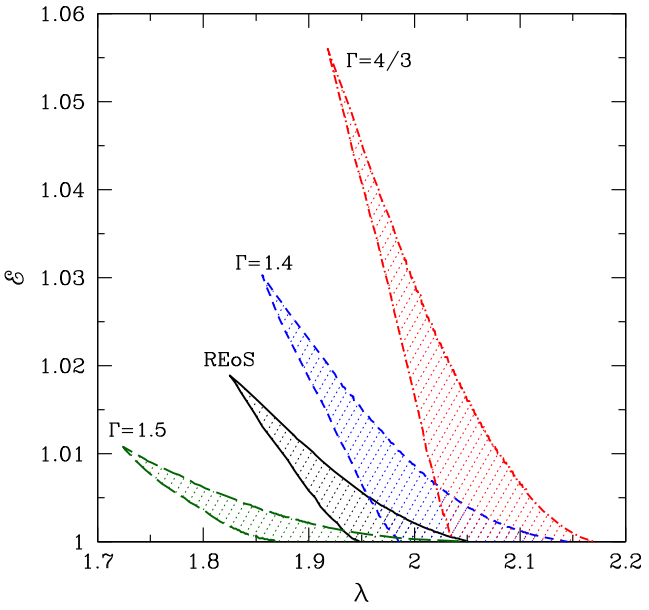


**Figure 4.** Parameter space for shock in $\lambda$–$\mathcal{E}$ plane. Region bounded with solid curve is for REoS and the same bounded by dot–dashed ($\Gamma = 4/3$), dashed ($\Gamma = 1.4$), and long-dashed ($\Gamma = 1.5$) are for IEoS. Here, we choose $a_k = 0.99$. See text for details.

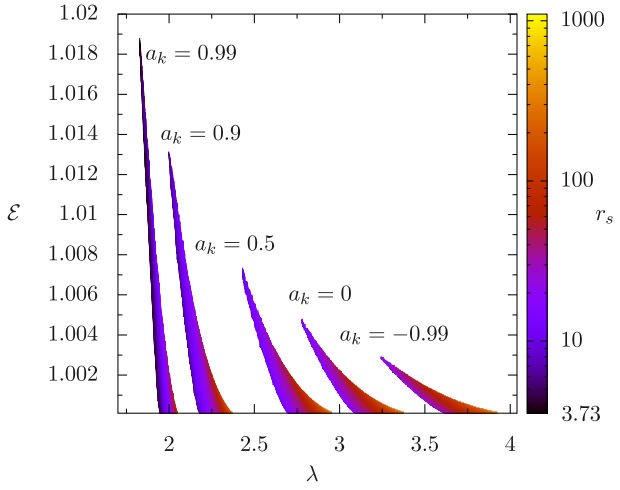


**Figure 5.** Two-dimensional projection of the three-dimensional plot of angular momentum ($\lambda$), energy ($\mathcal{E}$), and shock location ($r_{\rm s}$) for $a_k = 0.99$, 0.9, 0.5, 0 and $-0.99$ (left to right). In the right, vertical colour-coded bar denotes the range of $r_{\rm s}$ calculated for REoS. See text for details.

of the shock parameter space gradually shifts towards the lower angular momentum side as the spin of the black hole $a_k$ is increased. These findings are in agreement with the results of Aktar et al. (2015) and Kumar & Chattopadhyay (2017). From the figure, it is clear that shocks generally form close to the horizon for the rapidly rotating black holes ($a_k = 0.99$). Moreover, for a given $a_k$ and $\lambda$, shocks can also form at smaller radii when $\mathcal{E}$ is decreased. On the other hand, for fixed $a_k$ and $\mathcal{E}$, shocks, in general, settle down at larger radii for flows with higher $\lambda$. This clearly infers that centrifugal repulsion seems to play a crucial role in deciding the shock transition in the accretion disc.

Next, we demonstrate the shock parameter space in $\lambda$–$\mathcal{E}$ plane in terms of compression ratio ($R$) calculated using REoS. As before,

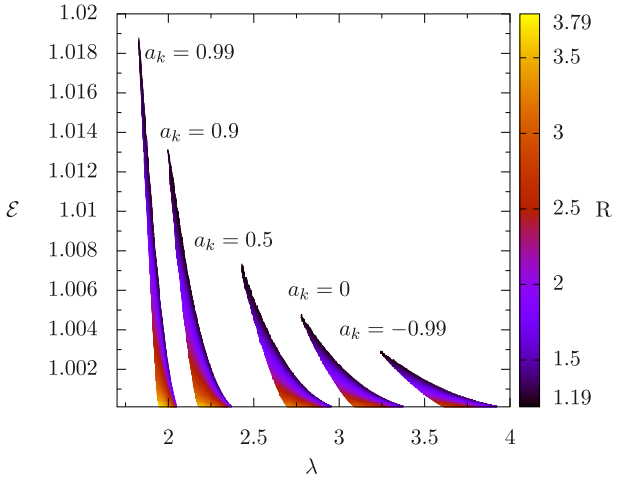


**Figure 6.** Two-dimensional projection of the three-dimensional plot of angular momentum ($\lambda$), energy ($\mathcal{E}$), and compression ratio ($R$) for $a_k = 0.99, 0.9, 0.5, 0$, and $-0.99$ (left to right). In the right, vertical colour-coded bar denotes the range of $R$ calculated for REoS. See text for details.

in Fig. 6, we examine the two-dimensional projection of the three-dimensional plot of $\lambda$, $\mathcal{E}$, and $R$, respectively, for $a_k = 0.99, 0.9, 0.5, 0$, and $-0.99$ (left to right) where vertical colour code indicates the range of $R$, where we find the minimum value of $R$ as $R^{\rm min} = 1.19$ and the maximum value of $R$ as $R^{\rm max} = 3.79$, respectively. Note that the effective region of the shock parameter spaces displayed here are exactly identical to Fig. 5. We observe that for a given $a_k$ and $\mathcal{E}$, inflowing matter experiences weak compression (i.e. $R \rightarrow 1$) when the angular momentum ($\lambda$) is relatively high and vice versa. On the other hand, for a given $a_k$ and $\lambda$, $R \rightarrow 1$ for flows with high $\mathcal{E}$ and vice versa. Overall, upon comparing Figs 5 and 6, it appears that $r_{\rm s}$ and $R$ are closely related for flows accreting around the rotating black holes.

### 4.5 $r_{\rm s}$–$R$ correlation and QPO frequency ($\nu_{\rm QPO}$)

In this section, we intend to explore an important aspect of shock waves in an accretion disc. We have already shown that accreting matter passes through the standing shock wave provided the shock conditions are satisfied. Interestingly, when the shock conditions are not favourable, but the entropy of the flow at the inner critical point ($r_{\rm in}$) is higher than the outer critical point ($r_{\rm out}$), shock front exhibits non-steady behaviour. This happens because of either resonance oscillation where infall time-scale becomes comparable to the post-shock cooling time-scale (Molteni et al. 1996) or dynamical oscillations where the flow viscosity above its critical limit triggers the unstable perturbation in the flow (Das et al. 2014). The nature of the shock oscillation generally yields as quasi-periodic, and the frequency of this QPO (Chakrabarti & Manickam 2000; Iyer et al. 2015) is computed as

$$\nu_{\rm QPO} = \frac{c/r_g}{\sqrt{2}\pi R r_{\rm s}\sqrt{r_{\rm s}-2}}, \tag{22}$$

where $r_g (= 2GM_{\rm BH}/c^2)$ denotes the Schwarzschild radius. Now, for a given set of input parameters, namely $\{\lambda, \mathcal{E}, a_k\}$, $r_{\rm s}$ and $R$ are uniquely determined and upon employing these values in equation (22), it is straightforward to estimate $\nu_{\rm QPO}$. Following this, we therefore retrace the shock parameter space in $r_{\rm s}$–$R$ plane in lieu of $\lambda$–$\mathcal{E}$ plane and in Fig 7, we display the two-dimensional projection of the three-dimensional plot of $\log(r_{\rm s})$, $R$, and $\log(\nu_{\rm QPO})$. In Fig. 7(a), results are obtained for $a_k = 0.0$ where we find $r_{\rm s}^{\rm max} = 999.3955$. Similarly, in Fig. 7(b), we choose $a_k = 0.99$ and obtain $r_{\rm s}^{\rm max} = 1071.5519$. For $M_{\rm BH} = 10\,{\rm M}_\odot$, we get $\nu_{\rm QPO}^{\rm max} = 77.68$ and 783.50 Hz corresponding to $a_k = 0.0$ and $a_k = 0.99$, respectively. In both panels, vertical colour-coded bar indicates the range of $\nu_{\rm QPO}$ in logarithmic scale. We observe that accretion flow exhibits HFQPOs when shock forms close to the horizon and vice versa irrespective to the black hole spin $a_k$. Interestingly, since the minimum value of the shock radius ($r_{\rm s}^{\rm min}$) decreases with $a_k$, the maximum QPO frequency is ascertained around extremely rotating black hole ($a_k = 0.99$).

It may be noted that in this work, we focus only on the axisymmetric shock oscillation model to explain the observed single peak HFQPO features. However, in reality, the shock can be non-axisymmetric as well that yields the spiral shock transition in the accretion flow. In fact, the shock transition between two-armed to three-armed spirals may be potentially viable to explain the 2:3 frequency ratio (Chakrabarti & Wiita 1993; Chakrabarti et al. 2009) as observed in some of the black hole sources (Belloni, Sanna & Méndez 2012; Motta 2016). However, the study of the non-axisymmetric behaviour of the accretion flow around the black hole is beyond the scope of this work.

## 5 ASTROPHYSICAL IMPLICATIONS

Recent observations confirm the significant detection of HFQPOs signature in few transient as well as persistent black hole sources (Altamirano & Belloni 2012; Belloni et al. 2012; Belloni & Altamirano 2013). In this section, we apply our formalism to explain the plausible origin of the HFQPO and its connection with the spin of the black hole sources. In doing so, we choose two well-studied Galactic black hole sources, namely GRS 1915+105 and GRO J1655−40, respectively and carry out the analysis in this section.

First, we consider the persistent black hole source GRS 1915+105 as its mass and spin are well constrained. Recently, Steeghs et al. (2013) estimated its mass as $M_{\rm BH} = 10.1 \pm 0.6\,{\rm M}_\odot$ and Miller et al. (2013) reported its spin value as $a_k = 0.98 \pm 0.01$. Using these fundamental properties of the source, it is straight forward to calculate the frequency of QPO ($\nu_{\rm QPO}$) from equation (22) for a given set of ($r_{\rm s}$, $R$). Since this source is known to exhibit HFQPOs (∼67 Hz; Morgan, Remillard & Greiner 1997; Belloni & Altamirano 2013), we self-consistently compute $r_{\rm s}$–$R$ correlation that yields $\nu_{\rm QPO} = 67$ Hz. In Fig. 8, we show the variation of $R$ as function of $r_{\rm s}$. In the figure, we consider the range of both mass and spin parameters as $9.5 \leq M_{\rm BH}/{\rm M}_\odot \leq 10.7$, and $0.97 \leq a_k \leq 0.99$ and the obtained results are displayed by the shaded region bounded by the solid curves. It is clear from the figure that HFQPOs observed in GRS 1915+105 can be understood using the present model provided shocks form close to the black hole ($7.5 \lesssim r_{\rm s} \lesssim 16$) having compression ratio ranging from weak ($R \sim 1.2$) to strong ($R \sim 3.6$) limit.

Next, we choose the transient black hole source GRO J1655−40. Several attempts have been made to obtain the precise measurements of mass and spin of GRO J1655−40. Using timing analysis, Motta et al. (2014) measured the black hole mass and spin as $M_{\rm BH} = 5.31 \pm 0.07\,{\rm M}_\odot$ and $a_k = 0.290 \pm 0.003$, respectively. Stuchlík & Kološ (2016) estimated the black hole mass in the range $5.1 < M_{\rm BH}/{\rm M}_\odot < 5.5$ and spin $a_k < 0.3$. Meanwhile, Shafee et al. (2006) calculated the spin of the black hole by spectral modelling in the range $0.65 < a_k < 0.75$. On the other hand, Aktar et al. (2017), recently constrained the range of the spin parameter as $a_k \geq 0.57$ by modelling the oscillation of PSC. Although mass of this source is

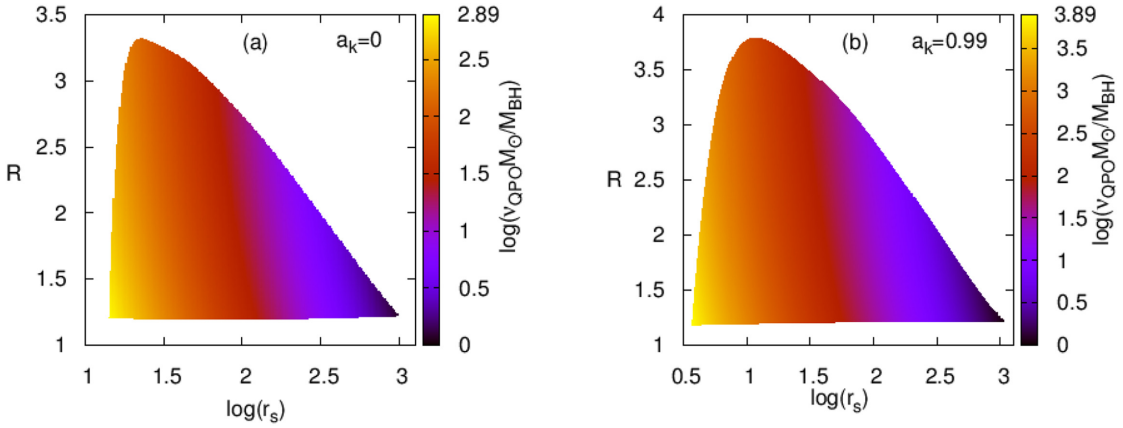


**Figure 7.** Two-dimensional projection of three-dimensional plot of $\{r_s, R, \nu_{QPO}(M_\odot/M_{BH})\}$ where vertical colour-coded bar indicates the range of QPO frequency in logarithmic scale. We choose $a_k = 0.0$ (a) and $a_k = 0.99$ (b). See text for details.

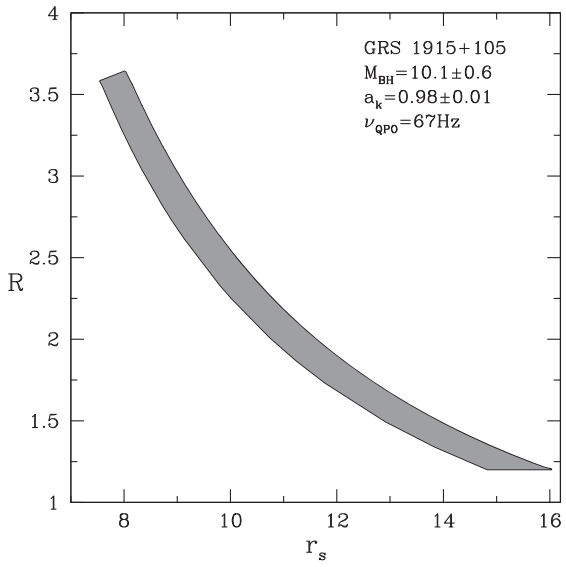


**Figure 8.** Variation of compression ratio ($R$) as function of shock location ($r_s$) that yields $\nu_{QPO} = 67$ Hz for Galactic black hole source GRS 1915+105. The ranges of $R$ and $r_s$ are obtained as the consequences of the mass and spin values as $9.5 \leq M_{BH}/M_\odot \leq 10.7$, and $0.97 \leq a_k \leq 0.99$, respectively. See text for details.

well constrained, however, all these studies indicate contradictory claims particularly in the context of spin measurement of the black hole source. To address this issue, we employ our formalism to calculate the HFQPO at $\nu_{QPO} = 450$ Hz which has been observed in GRO J1655−40 (Remillard et al. 1999; Strohmayer 2001; Aktar et al. 2017). Generally, this particular HFQPO is seen when the source resides in the anomalous state with high flux values as well as hardness ratio of 0.3–0.8 (Belloni et al. 2012). While computing the frequency of HFQPO ($\nu_{QPO}$), we choose $M_{BH} = 5.31\,M_\odot$ and freely vary all the input parameters $(\lambda, \mathcal{E})$ including spin $(a_k)$ of the black hole. With this, we find that GRO J1655−40 can exhibit HFQPO at 450 Hz provided its spin parameter $a_k \geq 0.85$ with $r_s \leq 6.9$ and $R \geq 1.22$.

## 6 CONCLUSIONS

Using the general relativistic approach, we study the shock induced global accretion solutions around Kerr black holes and compare the results obtained for the REoS as well as the IEoS. Accretion solutions of this kind are potentially viable as they can explain the observable properties of the black hole candidates. The main results of this work are summarized as follows.

(1) To the best of our knowledge, for the first time we find that there exists an upper limit of outer critical point location ($r_{out}^{max}$) for REoS whereas $r_{out}^{max}$ continues to remain unbound for IEoS. Since shock ($r_s$) forms in between $r_{in}$ and $r_{out}$ (i.e. $r_{in} < r_s < r_{out}$), the maximum shock radius ($r_s^{max}$) must be lower than $r_{out}^{max}$ and consequently, we observe an upper bound of $r_{out}^{max}$ as well for REoS (see Fig. 1).

(2) Considering both REoS and IEoS, we calculate the global transonic shocked accretion solutions for flows having identical input parameters around a black hole of spin $a_k = 0.99$ and find that solutions differ significantly (see Fig. 3). Further, we identify the range of parameters in $\lambda$–$\mathcal{E}$ plane that admits shock for REoS and IEoS (see Fig. 4). Here again, noticeable disagreement is seen. Since REoS satisfactorily describes the realistic accretion flow, we put emphasis on the accretion solutions yielded from REoS in order to study the observable properties of the black hole sources.

(3) In order to fit and compare the observed spectrum of the black hole sources, TCAF solutions are used as a local model in XSPEC software of HEASOFT (Debnath et al. 2014; Iyer et al. 2015) where shock location ($r_s$) and compression ratio ($R$) are treated as free model parameters. To check consistency, in this work, we examine the two-dimensional projection of three-dimensional plot of $\{\lambda, \mathcal{E}, r_s\}$ (see Fig. 5) and $\{\lambda, \mathcal{E}, R\}$ (see Fig. 6) as function of $a_k$. We find that for a given set of the input parameters $\{\lambda, \mathcal{E}, a_k\}$, $r_s$ and $R$ are determined uniquely and therefore, *we argue that these two quantities ($r_s$ and $R$) must not be chosen arbitrarily while fitting the observed spectrum of the black hole sources*. It may be noted that the ranges of $r_s$ and $R$ are obtained from our model calculation as: for $a_k = 0.0$: $14.1569 \leq r_s \leq 999.3955$ and $1.19 \leq R \leq 3.31$ and for $a_k = 0.99$: $3.7314 \leq r_s \leq 1071.5519$ and $1.19 \leq R \leq 3.79$.

(4) We specify that when shock conditions are favourable, shock front is expected to start exhibiting non-steady behaviour which is quasi-periodic in nature. We phenomenologically estimate the frequency of this QPO ($\nu_{QPO}$) of the shock front and retrace the shock parameter space in $r_s$–$R$ plane instead of $\lambda$–$\mathcal{E}$ plane where two-dimensional projection of three-dimensional plot of $\{r_s, R, \nu_{QPO}\}$ is displayed (see Fig. 7). We find that when shock oscillation takes place close to the horizon, it exhibits HFQPO. As shock can

form very close to the horizon for the rapidly rotating black holes, in this work, we find the maximum QPO frequency as $\nu_{\rm QPO}^{\rm max} = 783.50$ Hz for $a_k = 0.99$ and $M_{\rm BH} = 10\,{\rm M}_{\odot}$ (see Fig. 7).

(5) Finally, we employ our formalism to understand the plausible origin of the HFQPO and its linkage with the spin parameter considering two well studied Galactic black hole sources, namely GRS 1915+105 and GRO J1655−40, respectively. As the mass and spin of GRS 1915+105 are well constrained, we use these fundamental parameters to study the $r_{\rm s}$–$R$ correlation that yields the HFQPO at $\nu_{\rm QPO} = 67$ Hz. On the contrary, since the spin parameter of GRO J1655−40 remains an unsettled issue, we use our formalism to constrain spin of this source. We find that HFQPO at $\nu_{\rm QPO} = 450$ Hz can be explained in GRO J1655−40 provided it spins very rapidly with $a_k \geq 0.85$. This result is consistent with some of the earlier findings (Šrámková et al. 2015; Aktar et al. 2017).

At the end, we point out that this work is carried out considering some approximations. We ignore the effect of dissipations, namely viscosity, radiative processes, magnetic fields, etc. We also do not take into account of mass-loss from the accretion disc. Although the implementation of all these issues is beyond the scope of this work, however, the basic conclusion of this work is expected to remain unaltered due to the above approximations.

## ACKNOWLEDGEMENTS

Authors thank the anonymous reviewer for providing useful comments that significantly strengthened the manuscript. AN thanks GD, SAG, DD, PDMSA and Director, URSC for encouragement and continuous support to carry out this research.

## REFERENCES

Abramowicz M. A., Chakrabarti S. K., 1990, ApJ, 350, 281
Abramowicz M. A., Zurek W. H., 1981, ApJ, 246, 314
Aktar R., Das S., Nandi A., 2015, MNRAS, 453, 3414
Aktar R., Das S., Nandi A., Sreehari H., 2017, MNRAS, 471, 4806
Altamirano D., Belloni T., 2012, ApJ, 747, L4
Becker P. A., Kazanas D., 2001, ApJ, 546, 429
Belloni T., Psaltis D., van der Klis M., 2002, ApJ, 572, 392
Belloni T. M., Altamirano D., 2013, MNRAS, 432, 10
Belloni T. M., Sanna A., Méndez M., 2012, MNRAS, 426, 1701
Chakrabarti S. K., Manickam S. G., 2000, ApJ, 531, L41
Chakrabarti S., Titarchuk L. G., 1995, ApJ, 455, 623
Chakrabarti S. K. et al., 2009, Proc. of the 11th Marcel Grossmann Meeting on General Relativity, World Scientific. p. 569preprint (arXiv:0903.1482)
Chakrabarti S. K., 1989, ApJ, 347, 365
Chakrabarti S. K., 1990, Theory of Transonic Astrophysical Flows. World Scientific, Singapore
Chakrabarti S. K., 1996, ApJ, 464, 664
Chakrabarti S. K., 1999, A&A, 351, 185
Chakrabarti S. K., Das S., 2004, MNRAS, 349, 649
Chakrabarti S. K., Wiita P. J., 1993, ApJ, 411, 602
Chakrabarti S. K., Nandi A., Manickam S. G., Mandal S., Rao A. R., 2002, ApJ, 579, L21
Chattopadhyay I., Kumar R., 2016, MNRAS, 459, 3792
Chattopadhyay I., Ryu D., 2009, ApJ, 694, 492
Das S., 2007, MNRAS, 376, 1659
Das S., Chattopadhyay I., 2008, New Astron., 13, 549
Das S., Chattopadhyay I., Nandi A., Chakrabarti S. K., 2001a, A&A, 379, 683
Das S., Chattopadhyay I., Chakrabarti S. K., 2001b, ApJ, 557, 983
Das S., Chattopadhyay I., Nandi A., Molteni D., 2014, MNRAS, 442, 251
Debnath D., Chakrabarti S. K., Mondal S., 2014, MNRAS, 440, L121
Dihingia I. K., Das S., Mandal S., 2018, MNRAS, 475, 2164
Done C., Kubota A., 2006, MNRAS, 371, 1216
Esin A. A., McClintock J. E., Narayan R., 1997, ApJ, 489, 865
Frank I., King A. R., Raine D., 2002, Accretion Power in Astrophysics, Cambridge Univ. Press. Cambridge
Fukue J., 1987, PASJ, 39, 309
Fukumura K., Tsuruta S., 2004, ApJ, 611, 964
Fukumura K., Hendry D., Clark P., Tombesi F., Takahashi M., 2016, ApJ, 827, 31
Holzer T. E., 1977, J. Geophys. Res., 82, 23
Homan J., Belloni T., 2005, Ap&SS, 300, 107
Ingram A., Done C., 2011, MNRAS, 415, 2323
Iyer N., Nandi A., Mandal S., 2015, ApJ, 807, 108
Kato S., Wu X.-B., Yang L.-T., Yang Z.-L., 1993, MNRAS, 260, 317
Kim J., Garain S. K., Balsara D. S., Chakrabarti S. K., 2017, MNRAS, 472, 542
Kim J., Garain S. K., Chakrabarti S. K., Balsara D. S., 2018, MNRAS, 482, 3636
Kumar R., Chattopadhyay I., 2017, MNRAS, 469, 4221
Kumar R., Singh C. B., Chattopadhyay I., Chakrabarti S. K., 2013, MNRAS, 436, 2864
Lee S.-J., Chattopadhyay I., Kumar R., Hyung S., Ryu D., 2016, ApJ, 831, 33
Liang E. P. T., Thompson K. A., 1980, ApJ, 240, 271
Lu J. F., Gu W. M., Yuan F., 1999, ApJ, 523, 340
Mandal S., Chakrabarti S. K., 2005a, Ap&SS, 297, 269
Mandal S., Chakrabarti S. K., 2005b, A&A, 434, 839
Miller J. M. et al., 2013, ApJ, 775, L45
Molteni D., Ryu D., Chakrabarti S. K., 1996, ApJ, 470, 460
Morgan E. H., Remillard R. A., Greiner J., 1997, ApJ, 482, 993
Motta S. E., 2016, Astron. Nachr., 337, 398
Motta S. E., Belloni T. M., Stella L., Muñoz-Darias T., Fender R., 2014, MNRAS, 437, 2554
Nandi A. et al., 2018, Ap&SS, 363, 90
Nandi A., Debnath D., Mandal S., Chakrabarti S. K., 2012, A&A, 542, A56
Nishikawa K.-I., Richardson G., Koide S., Shibata K., Kudoh T., Hardee P., Fishman G. J., 2005, ApJ, 625, 60
Okuda T., Das S., 2015, MNRAS, 453, 147
Peitz J., Appl S., 1997, MNRAS, 286, 681
Remillard R. A., McClintock J. E., 2006, ARA&A, 44, 49
Remillard R. A., Morgan E. H., McClintock J. E., Bailyn C. D., Orosz J. A., 1999, ApJ, 522, 397
Riffert H., Herold H., 1995, ApJ, 450, 508
Ryu D., Chakrabarti S. K., Molteni D., 1997, ApJ, 474, 378
Sarkar B., Das S., 2016, MNRAS, 461, 190
Shafee R., McClintock J. E., Narayan R., Davis S. W., Li L.-X., Remillard R. A., 2006, ApJ, 636, L113
Shakura N. I., Sunyaev R. A., 1973, A&A, 24, 337
Steeghs D., McClintock J. E., Parsons S. G., Reid M. J., Littlefair S., Dhillon V. S., 2013, ApJ, 768, 185
Strohmayer T. E., 2001, ApJ, 552, L49
Stuchlík Z., Kološ M., 2016, ApJ, 825, 13
Suková P., Janiuk A., 2015, MNRAS, 447, 1565
Svensson R., Zdziarski A. A., 1994, ApJ, 436, 599
Tagger M., Pellat R., 1999, A&A, 349, 1003
Taub A. H., 1948, Phys. Rev., 74, 328
Titarchuk L., Osherovich V., 2000, ApJ, 542, L111
Yang R., Kafatos M., 1995, A&A, 295, 238
Šrámková E., Török G., Kotrlová A., Bakala P., Abramowicz M. A., Stuchlík Z., Goluchová K., Kluźniak W., 2015, A&A, 578, A90

## APPENDIX A: TYPICAL EXAMPLE OF ANGULAR MOMENTUM VARIATION

In an accretion disc around a black hole, the presence of viscosity is ubiquitous. However, the viscous time-scale generally exceeds the infall time-scale of the accreting matter at the inner part of the

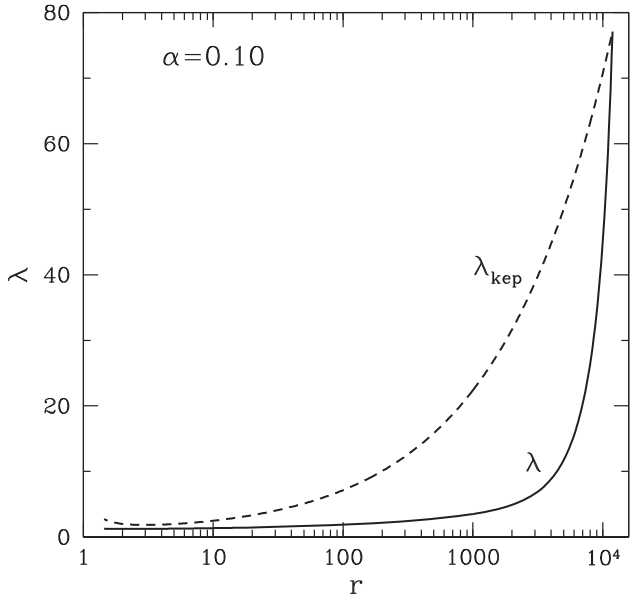


**Figure A1.** Variation of angular momentum ($\lambda$) of the accretion flow with radial coordinate ($r$) as shown by solid curve. Results depicted using dashed curve represent the Keplerian angular momentum distribution ($\lambda_{\rm Kep}$). Here, we use a unit system as $2G = M_{\rm BH} = c = 1$. See text for details given in Appendix A.

disc and therefore, matter does not get enough time to transport angular momentum outwards due to the differential motion leaving the flow to be inviscid in nature (Fukue 1987; Chakrabarti 1989). This particularly happens for accretion flow possessing multiple critical points. In Fig. A1, a typical example is depicted where we compare the angular momentum distribution ($\lambda$) for a viscous accretion solution (Chakrabarti & Das 2004) with the Keplerian angular momentum ($\lambda_{\rm Kep}$). In the figure, we inject accreting matter from the outer edge of the disc ($r_{\rm edge}$) with flow variables as $r_{\rm edge} = 11890.8$, angular momentum $\lambda_{\rm edge} = \lambda_{\rm Kep}$, velocity $v_{\rm edge} = 0.00064$, sound speed $a_{\rm edge} = 0.00688$, and viscosity parameter $\alpha = 0.1$, respectively. Fig. A1 clearly indicates that the angular momentum variation remains quite insensitive for wide range of inner radial coordinate. The above findings support the assumption of inviscid nature of accretion flow around the black hole.

## APPENDIX B: CALCULATION OF $\left.\frac{dv}{dr}\right|_c$

The gradient of radial velocity at the critical point given by

$$\left.\frac{{\rm d}v}{{\rm d}r}\right|_{\rm c} = \frac{N_1 - D_2 \pm \sqrt{(N_1 - D_2)^2 + 4D_1N_2}}{2D_1}, \tag{B1}$$

where,

$$N_1 = \frac{2a_{\rm s}^2}{\Gamma+1}(N_{11}+N_{12})A'\Theta_{11},$$
$$N_2 = N_{21}+N_{22}+N_{23}+N_{24}+N_{25}+N_{26},$$
$$D_1 = \gamma_v^2\left[1+\frac{2a_{\rm s}^2}{\Gamma+1}\left\{\frac{1}{v^2}-\frac{A'\Theta_{22}}{v}\right\}\right],$$
$$D_2 = -\frac{2a_{\rm s}^2\gamma_v^2A'}{(\Gamma+1)v}\Theta_{11},$$
$$N_{11} = \frac{\left(r-a_k^2\right)}{r\Delta}+\frac{5}{2r},\ N_{12} = -\frac{1}{2\mathcal{F}}\frac{{\rm d}\mathcal{F}}{{\rm d}r},\ N_{21} = \frac{2(r-1)}{(r-2)^2r^2},$$
$$N_{22} = -\frac{4a_K\lambda\gamma_\phi^2}{r^3\Delta}-\frac{2a_k\lambda\gamma_\phi^2\Delta'}{r^2\Delta^2}+\frac{4a_k\lambda\gamma_\phi\gamma_\phi'}{r^2\Delta},$$
$$N_{23} = -\frac{8a_k^2\gamma_\phi^2}{(r-2)r^3\Delta}-\frac{4a_k^2\gamma_\phi^2\Delta'}{(r-2)r^2\Delta^2}+\frac{8a_k^2\gamma_\phi\gamma_\phi'}{(r-2)r^2\Delta}-\frac{4a_k^2\gamma_\phi^2}{(r-2)^2r^2\Delta},$$
$$N_{24} = \Omega\gamma_\phi^2\lambda\frac{2a_k^2-(r-3)r^2\Delta'}{r^2\Delta^2}-\gamma_\phi^2\lambda\frac{2a_k^2-(r-3)r^2\Omega'}{r^2\Delta}$$
$$-2\lambda\Omega\gamma_\phi\frac{2a_k^2-(r-3)r^2\gamma_\phi'}{r^2\Delta}+2\lambda\Omega\gamma_\phi^2\frac{2a_k^2-(r-3)r^2}{r^3\Delta}$$
$$+\lambda\Omega\gamma_\phi^2\frac{r^2+2(r-3)r}{r^2\Delta},$$
$$N_{25} = \frac{2a_k\left(2a_k^2-(r-3)r^2\right)\Omega\gamma_\phi^2\Delta'}{(r-2)r^2\Delta^2}-\frac{2a_k\left(2a_k^2-(r-3)r^2\right)\gamma_\phi^2\Omega'}{(r-2)r^2\Delta}$$
$$-\frac{4a_k\left(2a_k^2-(r-3)r^2\right)\Omega\gamma_\phi\gamma_\phi'}{(r-2)r^2\Delta}+\frac{2a_k\left(2a_k^2-(r-3)r^2\right)\Omega\gamma_\phi^2}{(r-2)^2r^2\Delta}$$
$$+\frac{4a_k\left(2a_k^2-(r-3)r^2\right)\Omega\gamma_\phi^2}{(r-2)r^3\Delta}-\frac{2a_k\left(-r^2-2(r-3)r\right)\Omega\gamma_\phi^2}{(r-2)r^2\Delta},$$
$$N_{26} = \frac{2a_{\rm s}^2}{\Gamma+1}\left[N_{111}+N_{121}+(N_{11}+N_{12})A'\Theta_{11}\right],$$
$$N_{111} = -\frac{r-a_k^2}{r^2\Delta}-\frac{\left(r-a_k^2\right)\Delta'}{r\Delta^2}-\frac{5}{2r^2}+\frac{1}{r\Delta},$$
$$N_{121} = -4a_k^2r\frac{\left(a_k^2+r^2\right)\Delta'-4r\Delta}{\left(a_k^2+r^2\right)^4-4a_k^4\Delta^2},$$
$$A' = \frac{1}{\Theta}+\frac{\Gamma'}{\Gamma}-\frac{\Gamma'}{\Gamma+1}-\frac{a_{\rm s}^2(\Gamma+1)}{\Gamma\Theta},$$
$$\Theta_{11} = -\frac{2\Theta}{(N+1)}\left[\frac{\left(r-a^2\right)}{r\Delta}+\frac{5}{2r}-\frac{1}{2\mathcal{F}}\frac{{\rm d}\mathcal{F}}{{\rm d}r}\right],$$
$$\Theta_{22} = -\frac{2\Theta\gamma_v^2}{(N+1)v},\ \Omega = \frac{2a_k+\lambda(r-2)}{a_k^2(r+2)-2a_k\lambda+r^3}$$
$$\Gamma' = \frac{\partial\Gamma}{\partial\Theta}\ \text{and}\ \gamma_\phi' = \frac{\gamma_\phi^3}{2}\lambda\Omega'.$$

Here, all the quantities have their usual meaning.

This paper has been typeset from a TEX/LATEX file prepared by the author.